

Exploring the transformability of polymer-lipid hybrid nanoparticles and nanomaterial-biology interplay to facilitate tumor penetration, cellular uptake and intracellular targeting of anticancer drugs

Mohammad Ali Amini, Taksim Ahmed, Fuh-Ching Franky Liu, Azhar Z. Abbasi, Chesarahmia Dojo Soeandy, Rui Xue Zhang, Preethy Prashad, Carolyn L. Cummins, Andrew M. Rauth, Jeffrey T. Henderson & Xiao Yu Wu

To cite this article: Mohammad Ali Amini, Taksim Ahmed, Fuh-Ching Franky Liu, Azhar Z. Abbasi, Chesarahmia Dojo Soeandy, Rui Xue Zhang, Preethy Prashad, Carolyn L. Cummins, Andrew M. Rauth, Jeffrey T. Henderson & Xiao Yu Wu (2021) Exploring the transformability of polymer-lipid hybrid nanoparticles and nanomaterial-biology interplay to facilitate tumor penetration, cellular uptake and intracellular targeting of anticancer drugs, *Expert Opinion on Drug Delivery*, 18:7, 991-1004, DOI: [10.1080/17425247.2021.1902984](https://doi.org/10.1080/17425247.2021.1902984)

To link to this article: <https://doi.org/10.1080/17425247.2021.1902984>

 View supplementary material [↗](#)

 Published online: 30 Mar 2021.

 Submit your article to this journal [↗](#)

 Article views: 274

 View related articles [↗](#)

 View Crossmark data [↗](#)

 Citing articles: 5 View citing articles [↗](#)

ORIGINAL RESEARCH



Exploring the transformability of polymer-lipid hybrid nanoparticles and nanomaterial-biology interplay to facilitate tumor penetration, cellular uptake and intracellular targeting of anticancer drugs

Mohammad Ali Amini^{a,*}, Taksim Ahmed^{a,*}, Fuh-Ching Franky Liu^{a,*}, Azhar Z. Abbasi^a, Chesarahmia Dojo Soeandy^a, Rui Xue Zhang^a, Preethy Prashad^a, Carolyn L. Cummins^b, Andrew M. Rauth^c, Jeffrey T. Henderson^a and Xiao Yu Wu^a

^aAdvanced Pharmaceuticals & Drug Delivery Laboratory, Leslie Dan Faculty of Pharmacy, University of Toronto, Toronto, Ontario, Canada;

^bDepartment of Pharmaceutical Sciences, Leslie Dan Faculty of Pharmacy, University of Toronto, Toronto, Ontario, Canada; ^cDepartments of Medical Biophysics and Radiation Oncology, University of Toronto, Princess Margaret Cancer Centre, 610 University Avenue, Toronto, Ontario, Canada.

ABSTRACT

Background: Successful delivery of anticancer drugs to intracellular targets requires different properties of the nanocarrier to overcome multiple transport barriers. However, few nanocarrier systems, to date, possess such properties, despite knowledge about the biological fate of inorganic and polymeric nanocarriers in relation to their fixed size, shape and surface properties. Herein, a polymer-lipid hybrid nanoparticle (PLN) system is described with size and shape transformability and its mechanisms of cellular uptake and intracellular trafficking are studied.

Methods: Pharmaceutical lipids were screened for use in transformable PLN. Mechanisms of cellular uptake and the role of fatty acid-binding proteins in intracellular trafficking of PLN were investigated in breast cancer cells. Intra-tumoral penetration and retention of doxorubicin (DOX) were evaluated by confocal microscopy.

Results: The lead PLNs showed time-dependent size reduction and shape change from spherical to spiky shape. This transformability of PLNs and lipid trafficking pathways facilitated intracellular transport of DOX-loaded PLN (DOX-PLN) into mitochondria and nuclei. DOX-PLN significantly increased DOX penetration and retention over free DOX or non-transformable liposomal DOX particles at 4 h post-intravenous administration.

Conclusion: Transformability of PLN and lipid-biology interplay can be exploited to design new nanocarriers for effective drug delivery to tumor cells and intracellular targets.

ARTICLE HISTORY

Received 6 January 2021
Accepted 10 March 2021

KEYWORDS

Transformable size and shape; polymer-lipid hybrid nanoparticles; tumor penetration; cellular uptake; fatty acid-binding protein; intracellular trafficking

1. Introduction

Nanomedicine has found increasing importance and applications in the treatment of various diseases including cancer [1–5]. However, intravenous delivery of nanomedicine, e.g., nanoparticles (NPs), to their intracellular targets of solid tumors has to overcome a cascade of complex biological barriers. The first barrier is the reticuloendothelial system (RES) that removes foreign particles from the circulating blood (a macroscopic barrier). The second barrier involves the tumor microenvironment where elevated interstitial fluid pressure, disorganized vasculature, and dense extracellular matrix (ECM) hinder intratumoral transport of NPs. The third barrier is the cellular/sub-cellular barrier involving drug efflux transporters, lysosomal entrapment and degradation, and intracellular trafficking [3,6,7]. Overcoming these multi-stage barriers require varying properties of the nanocarriers at different stages. Yet, most drug loaded NPs are designed with

fixed properties largely aimed at bypassing the RES and enhancing tumor accumulation *via* passive or active targeting approaches. Such NPs frequently fail to provide efficient bioavailability of therapeutics at the cellular targets (e.g., mitochondria and nuclei) in solid tumors leading to therapeutic failure [3,6–9].

NPs have been extensively studied to delineate the mechanisms and explore strategies to circumvent the three above biological barriers. The general consensus of this research is that NP properties, such as size, shape, hydrophobicity, and surface charge play vital roles in the therapeutic efficacy of nanomedicine [6,7,10–12]. These properties can influence the biofate of NPs, such as blood circulation time, biomolecule binding, particle transport, cellular uptake, tumor penetration, and accumulation. Relatively large and spherical NPs with a hydrophilic coating of polyethylene glycol (PEG) result in prolonged systemic circulation, increasing the chance

CONTACT Xiao Yu Wu ✉ sxy.wu@utoronto.ca Advanced Pharmaceuticals & Drug Delivery Laboratory, Leslie Dan Faculty of Pharmacy, University of Toronto, 144 College Street, Toronto, Ontario M5S 3M2, Canada. Tel. 416-978-5272

*These authors have contributed equally.

 Supplemental data for this article can be accessed [here](#).

© 2021 Informa UK Limited, trading as Taylor & Francis Group

of tumor accumulation due to enhanced permeation and retention (EPR) effects. Smaller sized and less hydrophilic nanoparticles favor tissue penetration and cellular uptake [13–18]. However, if the size is too small (e.g., <5 nm in diameter), the particles can be cleared by kidney excretion; when the size is <50–100 nm in diameter, the particles can go to the liver through vascular fenestration [13,14]. Therefore, to prolong blood circulation and avoid unintended organ distribution, nanoparticles are prepared with ~100 – 150 nm diameters and hydrophilic surfaces [16,17].

In addition to particle size, particle shape can impact nanoparticle biofate. Compared to spherical particles, elongated and rod-shaped particles are likely to adhere more strongly to endothelial cell walls due to their large particle aspect ratios (length-to-width) [13,15]. They are less susceptible to phagocytosis and macrophage uptake [13,18]. They also tend to migrate toward blood vessel walls [19], thereby escaping maximal rates of blood flow and prolonging blood circulation time [7,13,20]. In contrast, spiky and elongated particles are more likely to penetrate deep into the tumor tissue and release drugs at therapeutic levels throughout the tumor cells [6,15,21].

The influence of NP particle size, shape, and surface properties on their biodistribution and tumor uptake has been delineated previously. But most of these studies were conducted using inorganic NPs with rigid and unchangeable structure (i.e., ‘hard’ NPs) that lack adaptability as drug carriers [10,11,13,15]. Only a few studies have demonstrated shape transformability of the NPs with limited *in vivo* evaluation [22–24]. Nanoparticles made of ‘soft’ hydrogel materials or cleavable surface chains have shown good circulation and tumor penetration [15,16]. Thus, ‘soft’ NPs such as bio-degradable and bio-compatible monolithic matrix (type 1) polymer-lipid hybrid NPs (PLN) may be a potential alternative nanopatform [3,25–27].

Our previous studies demonstrated superior capability of PLN systems for delivering synergistic drug combinations to overcome multidrug resistance in cancer cells and tumors, with profoundly reduced systemic toxicity of the anticancer drugs [25,28–34]. As a versatile nanocarrier, PLN could bypass multiple efflux-transporters (i.e., P-glycoprotein (P-gp), breast cancer resistance protein (BCRP), multidrug resistance-1 (MDR-1) and to significantly enhance cellular uptake and nuclear entry of DOX [35]. As a result, PLN enabled local bioavailability of the encapsulated drugs leading to increased tumor cell apoptosis and anticancer efficacy in breast tumor models as compared to free drug solution and commercially available ‘stealth’ liposomal DOX (Caelyx®), although, the latter exhibited longer blood circulation and greater tumor accumulation than PLN [35,36]. This difference in the *in vivo* efficacy was attributed to the difference in the intracellular drug release and drug trafficking. We further postulate that PLN may exploit special intracellular lipid transport pathways (e.g., fatty acid-binding protein, FABP) to deliver the drug to the target organelles. Thus, it is important to elucidate possible mechanisms of DOX delivery into intracellular targets [3,37–39].

In human triple-negative breast cancer cells, FABPs are up-regulated [40]. These FABPs facilitate trafficking of fatty acids, including esterified docosahexaenoic acid (DHA), oleic acid,

lauric acid, and stearic acid, into nuclei, mitochondria and lipid bodies [41,42]. In a recent study by our group, DHA was incorporated into the matrix of PLN which not only overcame membrane rigidity in multidrug resistant cancer cells, but also enhanced the mitochondrial reaction of co-delivered mitomycin C (MMC) [43]. These results suggest that the lipid composition of PLN can be selected to overcome cellular barriers and enhance organelle-specific intracellular delivery.

Herein, we aimed to explore 1) the transformability of DOX loaded PLNs under physiological conditions and 2) the lipid-FABP interaction and their possible impact on intracellular trafficking and localization. After screening different types of lipid, we constructed DOX-PLN that underwent changes with time from larger spheres to smaller ‘spiky’ particles due to differential dissolution rates of the constituent polymer and lipid. The transformability of PLN and fatty acid enhanced tumor penetration and retention of DOX in DOX-PLN were compared to non-transformable liposomal DOX (Caelyx® or Doxil®) *in vitro* and *in vivo*.

2. Materials and methods

2.1. Materials

DOX-HCl was purchased from MedChemExpress (Monmouth Junction, NJ, USA). Ethyl arachidate was purchased from TCI, Tokyo, Japan, and polyoxyethylene (100) stearate (Myrj® 59) from Spectrum Chemicals MFG Corp, Gardena, CA, USA. Nonionic block copolymer, Pluronic® F-68 (PF68) was a generous gift from BASF Corp. (Florham Park, NJ, USA). Hydrolyzed polymer of epoxidized soybean oil (HPESO) was synthesized using a published protocol with some modifications [44,45]. Poly(ethylene glycol)-coated (PEGylated) liposomal DOX (Caelyx®) was purchased from the pharmacy at the Princess Margaret Hospital (Toronto, ON, Canada). Cell culture medium α -modified minimal essential medium (α -MEM), fetal bovine serum (FBS), and phosphate buffered saline (PBS) were purchased from Gibco™ (Waltham, MA, USA). Myristic acid, stearic acid, polyoxyethylene (40) stearate (Myrj® 52) and all chemicals, unless otherwise stated, were purchased from Sigma-Aldrich Canada (Oakville, ON, Canada) and used without further purification.

2.2. Cell culture

Triple negative human breast cancer cells MDA-MB-231 (Wild type, WT) were purchased from ATCC (Manassas, VA, USA). Murine breast cancer EMT6 (WT) cells were originally obtained from Dr. Ian Tannock (Princess Margaret Cancer Center) and maintained in our laboratory. The cells were grown as a monolayer on T-75 flasks (Corning, Corning, New York, USA) in α -MEM (Gibco-Life Technologies, Burlington, ON, Canada) enriched with 10% FBS (Invitrogen Inc. Burlington, ON, Canada) and 1% penicillin-streptomycin cocktail (Gibco-Life Technologies, Burlington, ON, Canada) (growth medium) and incubated at 37°C in a humidified incubator with 5% CO₂ (NuAire DHD AutoFlow 5510, Hampton, NH, USA).

2.3. Preparation and characterization of the PLN

PLN were prepared in accordance with our previous work [35,44,45]. Briefly, a mixture of 50 mg of myristic acid (or other lipids, 50 mg added regardless of the molecular weight), 4 mg of polyoxyethylene (40) stearate (Myrj[®] 52), and 8 mg of polyoxyethylene (100) stearate (Myrj[®] 59) were melted in a 15-mL conical tube at 65°C. Once sufficiently homogenous, 400 μ L of DOX (12.5 g/L), 50 μ L of HPESO (50 g/L), 50 μ L of PF68 (100 g/L) were added to the mixture and left under stirring for 20 minutes. For blank PLN or fluorescein isothiocyanate (FITC)-labeled myristic acid PLN, 400 μ L of deionized water was used in place of DOX. The solution was then sonicated for 5 minutes at 80% peak amplitude of cycle 1- and 5-mm probe depth using a Hielscher UP100H probe ultrasonicator (Hielscher USA, Inc., Ringwood, NJ, USA). Finally, the entire emulsion was immediately transferred to 5 mL of deionized water stirring on ice. For intravenous (i.v.) use, the emulsion was instead transferred into the sterile 5% dextrose under stirring on ice.

2.4. Determination of particle size, polydispersity index (PDI), and zeta potential (ZP)

The polydispersity index (PDI), particle size, and zeta potential of PLNs were measured through dynamic light scattering (DLS) using a Zetasizer Nano-ZS (Malvern, England) at 25 °C. Nano-dispersions were diluted 1:100 with deionized water (Milli-Q[®], Millipore Sigma, Billerica, MA, USA) prior to measurement. To study PLN transformability, 1 mL of PLN was added to 9 mL of 0.05 M Tris buffer solution (pH 7.4) and incubated at 37°C under mild stirring. At predetermined time points (0, 1, 2, 4, 6, and 24 h), 1 mL of sample was withdrawn, and particle size was measured using DLS.

2.5. Transmission electron microscopy (TEM) for PLN

To investigate the morphology of PLN obtained at different time points, a small volume of particles (100 μ L) was taken from 0.05 M Tris buffer (pH 7.4) at 0, 1, 2, 4, 6, and 24 h, and diluted in distilled deionized water (DDI) (1 mL). The PLN solution (one drop, approximately 5 μ L) was pipetted onto a positively charged carbon coated copper grid and then dried under the bio-safety hood for 10–15 mins at room temperature. The TEM images were acquired on a Hitachi H7000 electron microscope (Mississauga, ON, Canada) with an accelerating voltage of 75 kV.

2.6. TEM analysis of cells

For TEM imaging, cells from different treatment groups were chemically fixed in polystyrene treated culture plates with 4% paraformaldehyde and 1% glutaraldehyde in 0.1 M phosphate buffer at pH 7.2 for 1 h. The cells were then post fixed with 1% osmium tetroxide in 0.1 M phosphate buffer at pH 7.2 for 20 min. The fixed cells were then dehydrated in a graded gradient ethanol series and embedded in Epon618. Ultrathin sections of embedded cancer cells were cut into 80–90 nm thickness and further stained with 5% uranyl acetate and 5% lead citrate for 10 min each. Finally, the stained sections were mounted onto TEM grids and were examined

by Hitachi H7000 electron microscope (Mississauga, ON, Canada) using an accelerating voltage of 100 kV.

2.7. Evaluation of the effect of PLN shape on cellular uptake

Fluorescently labeled PLN were prepared using cyanine5 (Cy5)-amine-conjugated myristic acid. PLN with different shapes were collected at different time points (0, 2, 4, 6, and 24 h) from the suspension in 50 mM Tris buffer (pH 7.4) at 37°C. These different shaped PLN were then used to treat MDA-MB-231 human breast cancer cells. Cells were cultured at a density of 500,000 cells per well for 1 h. After the required time, media was removed and cells were washed twice with PBS buffer, trypsinized and counted. From each treatment group (incubated with different-shaped PLN) around 10,000 cells were added to a 96-well plate in quintets. Fluorescence intensity of Cy5-amine was detected using a SpectraMax Gemini XS microplate reader (Molecular Device, Sunnyvale, CA), with an excitation wavelength of 630 nm and emission wavelength of 670 nm.

2.8. In vitro drug release studies

The rate of drug release from DOX-PLN as a function of pH was determined by a dialysis tube method. Two mL of PLN suspension (equivalent of 0.5 mg DOX/mL) or 0.5 mg/mL free DOX (as a control) were enclosed in a dialysis tube with 1 kD molecular weight cutoff (Spectrum Laboratories, Inc. Rancho Dominguez, California, USA). The sealed tubes were immersed in 500 mL of pH 5, 6.5 and 7.4 phosphate buffer at ionic strength 50 μ M in a United States Pharmacopoeia (USP)-grade type-2 dissolution apparatus (VanKel VK 7000, Edison, NJ, USA) at 37 \pm 0.5°C. The dissolution apparatus paddles were set to rotate at 50 rpm. At predetermined time intervals, 2 mL of release medium were withdrawn, and an equal volume of fresh medium was replaced to maintain the sink condition. The collected samples were then analyzed spectrophotometrically at 490 nm wavelength using an ultraviolet-visible (UV-Vis) spectrophotometer (Agilent 8453, Agilent Technologies, Santa Clara, CA USA).

2.9. Investigation of endocytosis mechanism of PLN

MDA-MB-231 and EMT6 cells were seeded in a 96-well plate (R&D systems, Minneapolis, MN, USA) at 10,000 cells per well and grown overnight at 37°C. Cells were then washed twice with PBS followed by equilibration in growth medium at 37°C or 4°C for 1 h. To examine the cell uptake mechanisms, cells at 37°C were pre-treated, in growth medium for 1 h, with 15 μ M of chlorpromazine and 450 mM of sucrose to inhibit clathrin-dependent endocytosis; 20 μ M of cytochalasin D to inhibit phagocytosis; and 10 μ g/mL nystatin to inhibit caveolin-dependent endocytosis, followed by the addition of FITC-labeled PLN suspension into each well.

At 4°C, cells were first treated with FITC-labeled PLN without addition of inhibitors. After 1 h, media was removed, and

the cells were washed twice with pre-warmed PBS; FITC fluorescence intensity was measured at excitation wavelength of 490 nm and emission wavelength of 520 nm using a SpectraMax Gemini™ XS fluorescence microplate reader (San Jose, CA, USA).

2.10. Intracellular fate of FITC-PLN

MDA-MB-231 or EMT6 cells (1×10^5) were seeded on 35 mm coated glass cover slips and were treated with 50 μ L of FITC-labeled PLN up to 4 h. Cells were then washed with fresh cell medium and stained with 1:5000 MitoTracker™ Deep Red FM (ThermoFisher Scientific, Eugene, OR, USA) and 1:5000 LysoTracker™ Red DND-99 (ThermoFisher Scientific, Eugene, OR, USA) for 10 minutes, respectively. Thereafter, the plates were washed with warmed PBS and fixed with 4% paraformaldehyde in PBS for 30 minutes, washed with PBS once, then imaged using a Leica SP8 CLSM. Detectors were set to $\lambda_{\text{excitation}}/\lambda_{\text{emission}}$ settings at 490 nm/520 nm (FITC-PLN), 577 nm/590 nm (LysoTracker™ Red DND-99), and 643 nm/779 nm (MitoTracker™ Deep Red FM). Co-localization of FITC-labeled PLN with cellular compartments was quantitated using Imaris (Zurich, Switzerland).

2.11. Analyses of intracellular localization of DOX-PLN

2.11.1. Western blotting for FABP7 expression

Pooled anti-FABP7 siRNA (Dharmacon, Inc. Colorado, USA) were transfected into cells using Lipofectamine 3000 as per manufacturer's instructions, harvested at 48 h and used for subsequent studies. Western blot was used to assess relative suppression efficiency using a 4–20% gradient gel to enhance separation of proteins. Cells were grown to approximately 70–90% confluency in a T-75 flask, counted, lysed using radio-immunoprecipitation assay (RIPA) buffer. Total protein concentration was normalized using a bicinchoninic acid (BCA) protein kit (ThermoScientific, Rockford, IL, USA) and samples reduced by boiling with β -mercaptoethanol immediately prior to loading. Accuracy of gel loading was assessed by blotting for β -actin in semi-quantitative comparison of relative protein expression.

2.11.2. Immunohistochemistry

MDA-MB-231 or EMT6 cells were plated at 1×10^5 on 35 mm coated glass cover slips, cultured overnight and were treated with 50 μ L of DOX-PLN emulsion for 4 h, followed by staining with 1:5000 MitoTracker™ Deep Red FM (ThermoFisher Scientific, Eugene, OR, USA) and 1:2500 Hoechst 33,342 (ThermoFisher Scientific, Eugene, OR, USA) for 10 minutes consecutively in order. Samples were washed in between each step with pre-warmed PBS and fixed with 4% paraformaldehyde in PBS for 30 minutes, washed with PBS once, then imaged using a Leica SP8 CLSM equipped with a 62 \times oil-immersion lens. All treatment groups were repeated for non-silenced (without FABP knockdown), and silenced cells (with FABP Knockdown) within each set in with scrambled control. Detectors were set to $\lambda_{\text{excitation}}/\lambda_{\text{emission}}$ settings at 410 nm/

498 nm (Hoechst 33,342), 490 nm/520 nm (FITC), 530 nm/590 nm (DOX), and 643 nm/779 nm (MitoTracker™ Deep Red FM). Co-localization of FITC-labeled PLN with cellular compartments was quantitated using Imaris (Zurich, Switzerland).

2.12. Intracellular uptake of polymer and lipid components of PLN

PLN were formulated as mentioned above, replacing respective reagents with Cy5-amine-labeled HPESO (excitation wavelength of 645 nm, emission wavelength of 665 nm), and FITC-labeled myristic acid (excitation wavelength of 490 nm, emission wavelength of 520 nm).

MDA-MB-231 or EMT6 cells were cultured overnight in 2 mL of α -MEM enriched on glass microscopy cover slips (Uncoated glass thickness No. 1.0 with glass diameter of 20 mm) (VWR, Radnor, PA, USA) at 37°C in a 5% CO₂. Next day 100 μ L of dye-labeled PLN were added to the dish for 1, and 24 h and were subsequently washed with warmed growth medium to remove free PLN. Cells were then analyzed using a confocal laser scanning microscope (CLSM) (Zeiss LSM 510 Carl Zeiss Canada, Ltd., Toronto, ON, Canada).

2.13. Orthotopic breast tumor model

All animal experiments were approved by the Animal Care Committee of University Health Network at the Ontario Cancer Institute and conducted in accordance with the Canadian Council on Animal Care guidelines. Female Balb/c mice (8 weeks old on receipt, Jackson Labs, USA) had free access to food (irradiated Tecklad LM485, Harland Tecklad, Indianapolis, IN, USA) and sterile water. Orthotopic breast tumors were inoculated by injection of 1×10^6 EMT6 murine breast cancer cells into right mammary fat pads. Mice were used for studies once the tumor size reached 150–200 mm³.

2.14. Intra-tumoral accumulation and penetration of DOX in breast tumor treated with various DOX formulations

EMT6 tumor-bearing Balb/c mice were treated with an i.v. injection of free DOX, Caelyx®, or PLN-DOX (200 μ L of DOX, 25 mg/kg of body weight). Animals were then sacrificed at 1, 4 or 24 h post treatment. Tumors were elicited and embedded in Optimal Cutting Temperature (OCT) compound (Tissue-Tek, Sakura Finetek, Torrance, CA, USA). Then liquid nitrogen was used to freeze and store the samples. For fluorescence imaging analysis, tumor tissue sections with 10 μ m thickness were prepared (Pathology Research Center, UHN, Toronto, ON, Canada). Tumor section slides were labeled with rat anti-CD31 and Alexa Flour 647-conjugated goat anti-rat IgG (1/1000 v/v) (Santa Cruz, CA, USA) for 1 h per the supplier's instructions. The fluorescence intensity of DOX ($\lambda_{\text{excitation}}/\lambda_{\text{emission}}$ settings = 480 nm/570 nm), and CD31 ($\lambda_{\text{excitation}}/\lambda_{\text{emission}}$ settings = 650 nm/665 nm) were quantified by imaging the slides using an Olympus BX50 microscope equipped with a mercury light source and an Olympus UplanSApo 10X/

0.40 objective lenses. DOX-positive areas within a viable tumor region were quantified using ImagePro software (Media Cybernetics Image Pro PLUS, Rockville, MD, USA). A minimum intensity threshold was used to minimize noise from tissue auto fluorescence. DOX penetration into tumor tissue relative to tumor vasculature was quantified using CD31-positive overlays using Metamorph software (7.7.2.0 version, Molecular Devices, San Jose, CA, USA). A custom MATLAB (MathWorks, Natick, MA) program was developed in house for the composite image analysis. Briefly, to detect the location of blood vessels, a binarized image of CD31-positive pixels was obtained. This information was then used to create a distance map of the entire image. In this process each pixel in the tissue section is represented by its distance in microns to the nearest blood vessel. To create a composite image containing distance measurements of DOX-positive pixels from blood vessels, a binary mask of DOX-positive areas was combined with the distance map. The signal of DOX in the blood vessels was set as 100% and the data are presented as the percent of DOX signal in the tumor tissue at each distance from the nearest blood vessel vs that in the blood vessel. Non-viable/necrotic tumor regions were omitted from analysis.

3. Results and discussion

3.1. PLN transformability

There has been growing interest in evaluating the effect of different materials on engineering NPs with precise size, shape, surface charge, elasticity and surface functionality to improve their bioavailability and efficacy [10,11]. In this study, different PLN formulations are developed based on the chemical composition. For this purpose, different lipids, fatty acids (myristic acid and stearic acid), and arachidonic acid ethyl ester (Figure 1A) were used to explore their effect on the geometric changes of the PLN. Variation in the size and shape of the particles were monitored as a function of time under physiological conditions. As can be seen in (Figure 1A), the average size of the myristic acid-based PLN formulation was reduced from 150 nm to 85 nm within 24 h in Tris buffer pH 7.4 at 37°C (Figure 1A) with zeta potential values ranging between -29.3 and -22.5 mV (supplementary information (SI) Figure S1). Interestingly, this particle size change is also accompanied by a change in geometry of PLN, as depicted by the TEM images in (Figure 1B). The original spherical shape of the myristic acid-based PLN transforms into a 'spiky' shape after 6 h of incubation. In contrast, the size and shape of PLN prepared using other lipids (e.g., stearic acid and ethyl arachidate) remained stable for 48 h in Tris buffer pH 7.4 (Figure 1A and SI Figure S2).

The changes in particle shape in myristic acid-based PLN but not in other two types of lipid-based PLNs may be ascribed to the difference in the chemical structures of the lipids and their physicochemical interaction with the polymer HPESO. As illustrated in SI Figure S3, HPESO, synthesized by hydrolyzing ring-opening polymerized epoxidized soy bean oil [30], consists of several (7–10) fatty acid chains linked by

ethylene oxide bond ($-\text{CH}_2-\text{CH}-\text{O}-$). Most of the fatty acid chains in the HPESO are C18 and some are C16. Therefore, it is postulated that the lipids with longer aliphatic chains like stearic acid ($\text{C}_{18}\text{H}_{36}\text{O}_2$) (C18) and ethyl arachidate ($\text{C}_{22}\text{H}_{44}\text{O}_2$) (C20) would align better with the fatty side chain of HPESO, forming stronger lipid domains with incorporation of the polymer chains than myristic acid ($\text{C}_{14}\text{H}_{28}\text{O}_2$) (C14). Since all these studied lipids can form hydrogen bonds with the carboxylic group of HPESO (SI Figure S3), the difference between these lipids in the aliphatic chain length and extent of hydrophobic interaction with HPESO governs the strength of and integrity of the polymer-lipid matrix. The lipids with longer aliphatic chains, i.e., stearic acid and ethyl arachidate, have stronger hydrophobic interaction and partitioning with HPESO making a more stable polymer-lipid matrix in an aqueous medium. This explains why a stable spherical morphology of stearic acid- and ethyl arachidate-based PLNs remained even after 24 h dissolution test (SI Figure S2). In contrast, the shorter C14 aliphatic chain of myristic acid can only hold a part of fatty side chain of HPESO. Therefore, when the myristic acid-based PLN was exposed to an aqueous medium, the interaction between water and the hydrophilic groups (i.e. $-\text{CH}_2-\text{CH}-\text{O}-$) and $-\text{COO}-$) in the HPESO prevails the hydrophobic interaction, gradually pulling the polymer out from the PLN, leaving behind smaller, rougher, and spiky lipid-rich particles. The detailed molecular mechanisms of the system may be further elucidated by physicochemical and thermodynamic characterizations [46] and molecular dynamics modeling [47,48].

The transformable myristic acid-based PLN was selected for further studies of cellular uptake in relation to particle properties. The distribution of PLN inside cancer cells was examined using TEM of MDA-MB-231 cells following incubation with PLN for 1 and 24 h (Figure 1C and SI Figure S4). At 1 h, PLNs with sizes from 80 nm to 120 nm are internalized into the cells and are seen in vesicles suggesting involvement in endocytosis (Figure 1C, SI Figure S4). In addition, more PLNs are found close to the nucleus as compared to the liposomal DOX (Caelyx®). Consistent with the result of PLN shape change under physiological conditions, the TEM image of cells following the 24 h incubation with PLN showed shape transformation inside the cells from spherical to spikey shape. Interestingly, many of these spiky-shaped particles were seen within mitochondria and nuclei (Figure 1C and SI Figure S4). SI Figure S4 presents further enlarged TEM images of cells for greater clarity. In contrast, the commercially available liposomal DOX (Caelyx®) did not exhibit any change in particle shape, and mostly stayed in the cytoplasm and endosomes (Figure 1C and SI Figure S4) similar to prior findings [16]. The surface PEGylation in Caelyx® improves the stability of liposomes, however, it increases the hydrophilicity of these liposomes resulting in reduced cellular uptake and poor endosomal escape [16].

To further investigate whether the observed changes in size and shape of PLN would influence their cellular uptake, different shaped, fluorescent-labeled PLN were collected from the suspension incubation under physiological conditions at different time

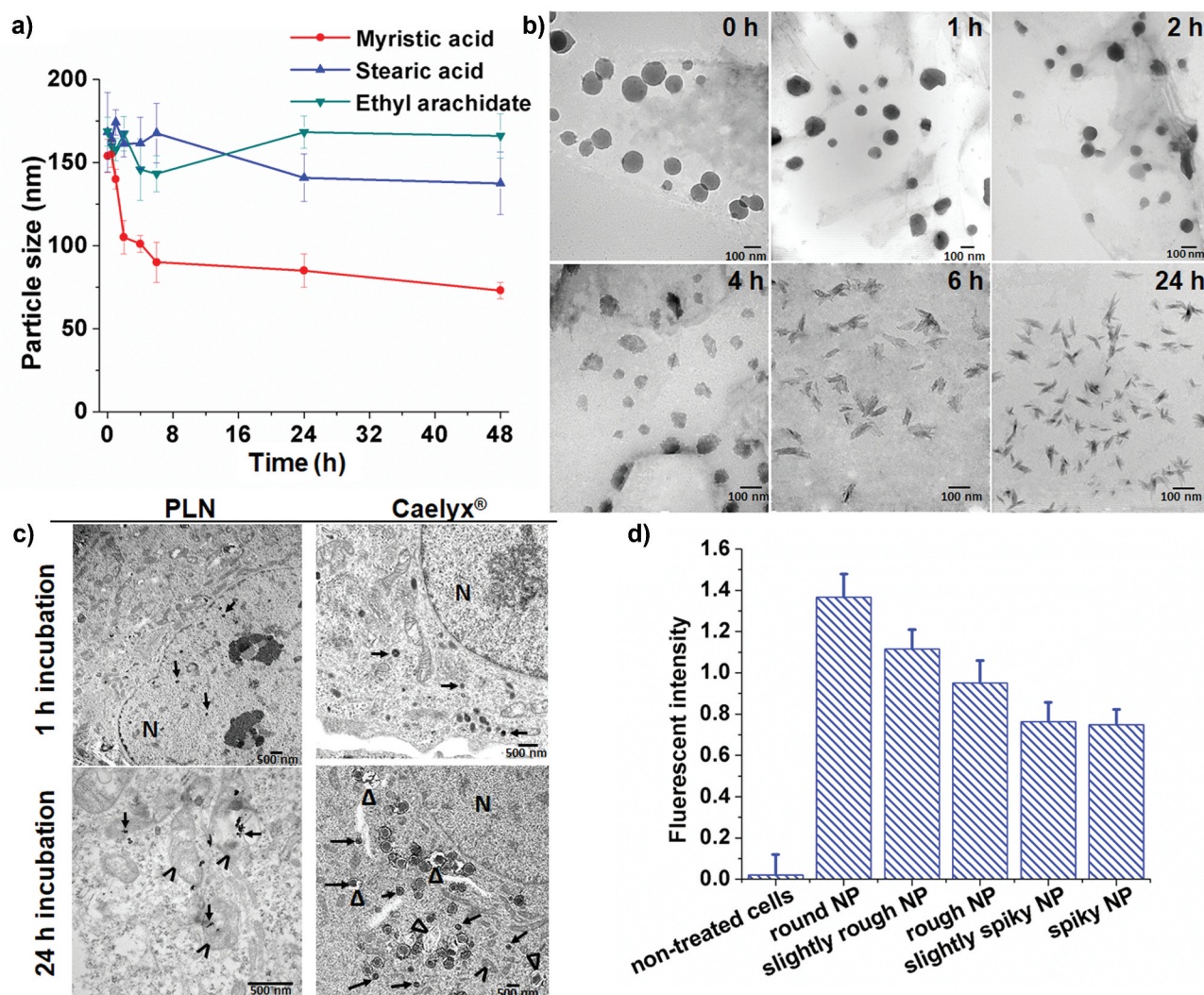


Figure 1. Effects of lipid type on particle size and cellular uptake of PLN. A) The particle diameter of the PLN formulation obtained using different materials at different time points in 0.05 M Tris buffer solution (pH 7.4) at 37°C using DLS. Data are presented as the mean \pm SD ($n = 3$). B) TEM images of myristic acid-based PLN obtained at different time point from Tris buffer solution (pH 7.4) at 37°C under mild stirring. The particles sampled before (0 h), and during stirring at 1, 2, 4, 6, and 24 h. Scale bar = 100 nm. C) TEM images of MDA-MB-231 cells incubated with PLN (first column) and liposomal DOX, Caelyx[®] (second column) for 1 and 24 h at 37°C. Letter 'N' indicates nuclear region. Black arrows point to lipid component from the nanoparticles or liposomes; arrow heads point to mitochondria; and triangles point to endosomes. D) Cellular uptake of PLN with different shapes in MDA-MB-231 cells after 1 h incubation at 37°C in growth medium. Different shaped PLNs were collected at 0, 2, 4, 6 and 24 h from 0.05 M Tris buffer (pH 7.4). Data are presented as the mean \pm SD ($n = 3$). SD: Standard deviation, NP: nanoparticle.

points, e.g. round (0 h), slightly rough (2 h), rough (4 h), slightly spiky (6 h), and spiky (24 h). These different shaped PLNs were then incubated with MDA-MB-231 cells for 1 h at pH 7.4 and 37°C. As shown in (Figure 1D), 'round'- PLNs exhibited a 1.8-fold higher cellular uptake compared with spiky-shaped PLNs.

A similar observation was reported for gold NPs (surface coated with cetyl trimethylammonium bromide, CTAB and transferrin), where spherical particles showed greater cellular internalization than the rod-shaped particles [49,50]. In contrast, a polystyrene NP coated with the targeting antibody trastuzumab also demonstrated shape dependent enhanced cellular uptake, where rod-shaped NPs exhibited higher specific uptake in human breast cancer MDA-MB-231 cell line, when compared to spherical NPs uptake in HER2+ human breast cancer cells (BT-474 and SK-BR-3) as well as HER2-cells (MDA-MB-231) [51]. These results were attributed to the unique role of shape which governed the binding and

release of NPs at the cell surface [51]. Thus, literature review reports contradictory results on the efficacy of shape-dependent cellular uptake when comparing spherical NPs with elongated NPs [10]. The contradictory results may suggest that the nanocarrier materials, e.g., polymers, lipids, or inorganic materials may play an important role in cellular uptake and influence the therapeutic outcome of drug cargo.

3.2. pH-dependent drug release from PLN

Tumor microenvironments typically possess distinct characteristics (e.g., hypoxia and acidic pH, ~ 6.5) [52], which have previously been exploited for preferential drug release from NPs [3,53]. Therefore, *in vitro* drug release kinetic studies were conducted with the DOX-PLNs and compared with free DOX using a dialysis-based drug release method (SI Figure S5).

A burst release of free DOX was clearly observed during the first 1 h in the acid buffer, whereas the release was little slow at the neutral pH (~7.4). Similarly, DOX-PLNs also demonstrated a pH-dependent sustained drug release in which higher drug release was observed at lysosomal pH (~5), compared to the tumor microenvironment (pH ~6.5) or physiological pH (~7.4). As can be seen from SI Figure S5, within 4 h free DOX was released at levels of approximately ~94%, ~81% and ~78% at pH 5, 6.5 and 7.4, respectively. In contrast, only about ~41%, 11% and 8% of DOX was released from PLN at pH 5, 6.5 and 7.4, respectively, indicating a strong pH-dependent drug release from PLN. This preferential DOX release from PLN at the tumor microenvironmental pH and the lysosomal pH could help drug targeting to tumor cells and enhance drug efficacy, while significantly reducing off-target toxicity. In this DOX-PLN system, the polymeric component is responsible for the ionic complexation and lipid partition of DOX. The -COOH groups in HPESO undergo protonation at acidic pH, which weakens their binding with DOX, facilitating faster DOX release from the PLN at intratumoral and lysosomal pH, compared to physiological pH [46,53–55].

3.3. Mechanism of *in vitro* cellular uptake of PLN

Endocytosis pathways are the most important mechanisms governing the internalization of NPs into cells. Endocytic uptake of NPs is governed by their size, surface chemistry and shape [52,56]. In addition, NP size also affects endocytosis mechanism, e.g., polymeric NPs < 200 nm undergoes clathrin-dependent endocytosis whereas, an increase in particle size from 200 to 500 nm promotes caveolae-mediated internalization [11,56,57]. In order to elucidate the uptake mechanism of PLNs in EMT6 and MDA-MB-231 cells, cells were pre-treated with sucrose and chlorpromazine to inhibit clathrin-mediated endocytosis, cytochalasin-D to inhibit phagocytosis, and nystatin to inhibiting caveolae-dependent endocytosis. The obtained results are presented in (Figure 2A and D). Cells incubated with FITC-labeled PLN at 4 °C showed lower FITC fluorescence intensity than those treated at 37 °C, suggesting energy-dependent internalization of FITC-PLN. A similar trend in both EMT6 and MDA-MB-231 cells suggests that the cellular uptake of PLN is an active transport process, common in different breast tumor cell lines [53]. Nevertheless, MDA-MB-231 cells exhibited 30% more PLN uptake after 1 h incubation at 37°C, when compared to EMT6 cells. Furthermore, a significant change in uptake was observed only with the administration of hypertonic sucrose (known to disrupt clathrin lattices within endocytic vesicles) and chlorpromazine to both cell lines, implying that PLN uptake is likely through clathrin-mediated endocytosis (Figure 2A and D). Similar observations have been reported for acetylated rapeseed protein isolate (ARPI), chitosan and DOX-based PLN system, which showed clathrin-dependent endocytosis in MDA-MB-231 and MCF-7 cells [53].

CLSM analysis of intracellular localization of FITC-PLN as a function of time was performed using FITC-labeled PLN (FITC-PLN, green), LysoTracker™ to stain lysosomes (yellow), and MitoTracker™ to stain mitochondria (red). As depicted in

Figure 2B & 2E, the FITC-PLN was initially located in lysosomes and gradually moved to mitochondria and nuclei with time. Quantitation of fluorescence signal co-localization of FITC-PLN demonstrated enhanced mitochondrial and nuclear uptake of FITC-PLN over time for both EMT6 (Figure 2C) and MDA-MB-231 cell lines (Figure 2F). These results suggest that PLN escaped the lysosomal entrapment, and preferentially accumulated in mitochondria and nuclei over time. Given that DOX is a potent DNA topoisomerase II inhibitor in mitochondria and the role which these organelles play in cellular energetics [58], accumulation of PLN in the mitochondria and nucleus could be an additional benefit in targeting and killing cancer cells.

3.4. Elucidating intracellular trafficking mechanisms of DOX and fatty acid

Various approaches have been exploited to increase drug uptake and accumulation, such as using nanocarrier to bypass drug efflux protein-mediated MDR [3]. However, trafficking endocytosed drug to its pharmacological targets (e.g., nucleus and mitochondrion) may require different transport mechanisms. To investigate the intracellular trafficking of DOX in DOX-PLN, and its possible mediation by FABPs, we examined the intracellular transport of DOX-PLN in MDA-MB-231 cells by CLSM with the postulation that FABP-overexpressing breast cancer cells would facilitate preferential cargo localization into cell nuclei.

The study revealed differences in DOX localization inside cell compartments between DOX-PLN or free DOX treated wild type (WT) cells (Figure 3A, top two panels), as well as between WT and FABP7 knockdown (KD) cells incubated with DOX-PLN (Figure 3A, middle and bottom panels). A significant amount of DOX-nucleus co-localization was observed for DOX-PLN formulation when compared to the free DOX, as confirmed by the co-localization analysis (Figure 3C).

Quantitative co-localization analysis of fluorescent images was further performed using Pearson's correlation coefficients (PCC) to determine covariance of the two signals (R^2). The R^2 values closer to 1 indicate greater overlap of groups A and B, and 0 indicating a lack of correlation between these groups, whereas, a value of -1 demonstrating a perfect inverse correlation (i.e., active avoidance of two signals) [59]. As seen in (Figure 3C), PCC values were in the range of 0.5 for free DOX to mitochondria vs a negative correlation with respect to the nucleus. In contrast, DOX-PLN treated cells exhibited a significantly higher correlation of DOX with the nucleus than the mitochondrion. Thus, the inverse relationship in DOX-mitochondrial to DOX-nuclear co-localization demonstrates the change in DOX transport by the PLN which directly delivers DOX into cell nuclei (Figure 3A and C). In FABP7 KD cells, the nuclear uptake of DOX was not altered noticeably, whereas the mitochondrial uptake of DOX was significantly reduced (Figure 3C). The negative correlation of DOX in DOX-PLN to mitochondria upon FABP7 KD implies the possible involvement of FABP7 in mediating the intracellular trafficking mechanism in DOX-PLN transport to the mitochondria.

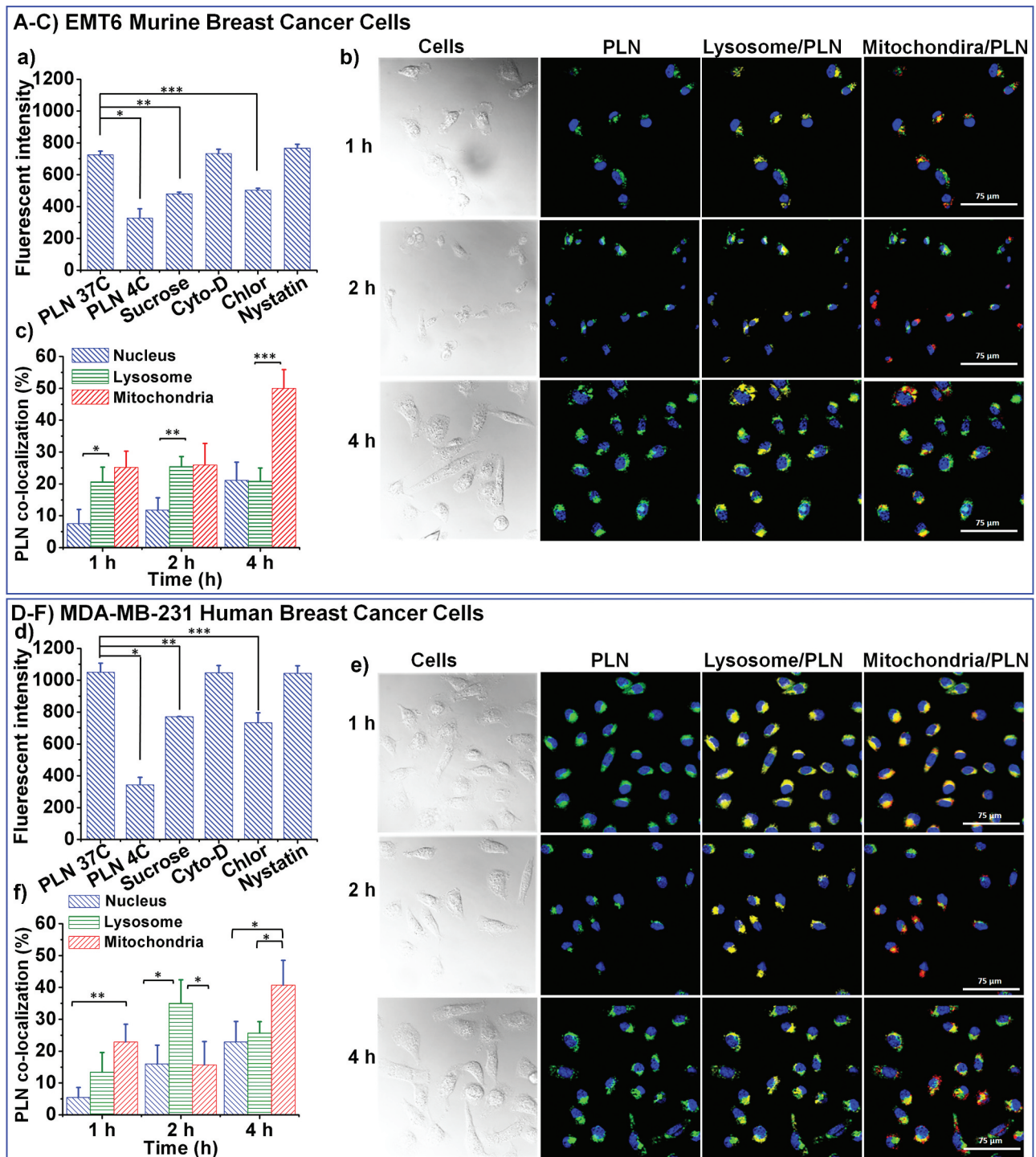


Figure 2. Mechanism of cellular uptake and intracellular localization of PLN. A – C) EMT6 cells and D – F) MDA-MB-231 cells. The EMT6 (A) and MDA-MB-231 (D) cells were treated with different endocytosis inhibitors, e.g., clathrin (chlorpromazine and sucrose), phagocytosis (cytochalasin D), and caveolin (nystatin) for 1 h prior to incubating FITC-labeled PLN for 1 h at 37°C, and cellular internalization was quantified using fluorescent spectroscopy. Cells were also incubated at 4°C to compare with the uptake of FITC-PLN at 37°C. Data are presented as the mean \pm SD (n = 3). Intracellular trafficking of FITC-labeled PLN in EMT6 (B) and MDA-MB-231 cells (E) upon incubation with the cells for 1, 2, and 24 h. Confocal microscopy was used to determine FITC-labeled PLNs (stained as green) distribution in subcellular organelles. Cell nuclei were stained blue with DAPI, late endosome/lysosomes were stained with LysoTracker™ (yellow), and mitochondria were stained with MitoTracker™ (red). Scale bar = 75 μ m. C) Fluorescence signals for the channel overlap of FITC-labeled PLN with lysosomes and mitochondria in EMT6 and MDA-MB-231 (F) were quantified. All the data are presented as mean \pm standard deviation (SD) (n = 3). *p < 0.05; **p < 0.01.

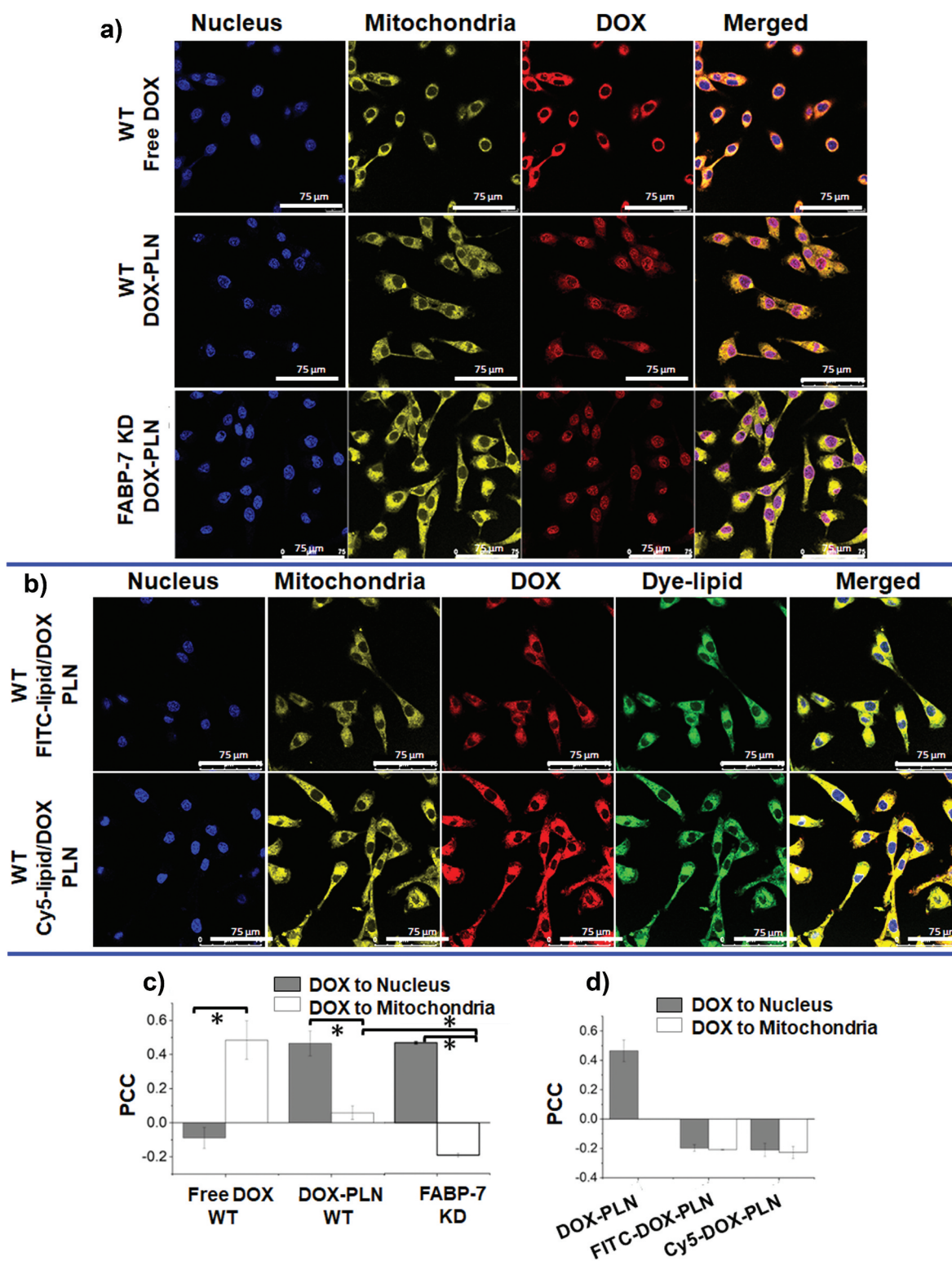


Figure 3. Effect of lipids on intracellular trafficking of DOX loaded PLNs in MDA-MB-231 cells using CLSM. A) Comparison of co-localization of free DOX and DOX-PLN in MDA-MB-231 cells after incubation for 4 h (top two rows, respectively). Bottom row: Influence of FABP7 knockdown on intracellular DOX distribution in MDA-MB-231 cells incubated with DOX-PLN for 4 h. Scale bar = 75 μ m. B) Effect of lipids (after conjugating lipids with fluorescent dye) on intracellular trafficking of PLNs. MDA-MB-231 cells were treated with FITC-labeled myristic acid-based DOX-PLN (top row) and Cy5-labeled myristic acid-based DOX-PLN (bottom row) for 4 h. Images were taken using a CLSM. Cell nuclei were stained with DAPI (blue), mitochondria were stained with MitoTracker™ (yellow), red color was used for DOX, and green color was used for FITC or Cy5-labeled myristic acid. Scale bar = 75 μ m. All cells images were taken using a CLSM. C) and D) Co-localization analysis from the obtained CLSM images. C) PCC of images of internalized free DOX and DOX-PLN in nucleus and mitochondria of WT MDA-MB-231 cells or FABP7-KD MDA-MB-231 cells. DOX-PLN delivered more DOX to nuclei than free DOX alone ($p = 0.0003$), but less into mitochondria ($p = 0.0084$). D) PCC of images of internalized DOX-PLN, FITC-labeled myristic acid-based DOX-PLN and Cy5-labeled myristic acid-based DOX-PLN to nucleus and mitochondria of WT MDA-MB-231 cells. Anti-correlation was observed for Dye-DOX-PLN to nuclei than DOX-PLN. All error bars were constructed with standard error. WT: wild type; KD: Knockdown. All data are presented as mean \pm SD ($n = 3$). * $p < 0.05$.

It is speculated the terminal carboxylate group on myristic acid is the major moiety that binds to the FABP proteins. We, therefore, examined if conjugating a dye molecule at the terminal carboxylate end of myristic acid would impact intracellular trafficking of drug cargo (referred to as the 'capping hypothesis'). To this end, intracellular trafficking of the DOX-PLN system was examined using CLSM by replacing the blank myristic acid with dye conjugated myristic acid in the DOX-PLN (thus 'capping' the carboxylate group of myristic acid reducing its binding affinity of FABP7). Co-localization of DOX within cell nuclei was used to track the differences in DOX distribution. Representative images from these two analyses are shown in (Figure 3B) with accompanying co-localization shown in (Figure 3D). As seen in (Figure 3B), by capping the -COOH group of myristic acid by FITC or Cy5 conjugation resulted in significant decrease of DOX uptake in nucleus, with associated negative PCC values (Figure 3D). In comparison to DOX-PLN, FITC-DOX-PLN ($p < 0.0001$) and Cy5-DOX-PLN ($p < 0.0001$) did not deliver detectable DOX to the nucleus. These results demonstrated that by capping the carboxylate group of myristic acid with FITC or Cy5 dye molecules prevents the ligand binding of PLN to the arginine-rich domains of FABP proteins on the MDA-MB-231 cancer cells.

Taken together with all the above results, we speculate that there may be multiple pathways involved in the intracellular trafficking of DOX to the nucleus beyond FABP7. Additionally, a modest 40–50% KD of FABP7 was achieved with siRNA transfection ($p = 0.0217$) (SI Figure S6), which makes it difficult to precisely determine whether there is a strong role of FABP7 in nuclear trafficking due to the marginal KD. Intriguingly, the observed DOX-nuclear anti-/non-correlation with FITC-DOX-PLN and Cy5-DOX-PLN may suggest that the free -COOH in lipids is likely responsible for recognition by the molecular lipid trafficking mechanisms to deliver DOX into cell nuclei. It is possible that the limited KD of FABP7 might have affected the DOX-nuclear co-localization. In addition, there may be compensatory pathways, such as FABP5 found in mammary cells or protein kinase C also implicated in EGFR activation in tumors. Blocking the carboxylate group on myristic acid by esterifying it with a bulky moiety, sterically hindering binding to the arginine-rich active domain of FABP7 led to a decrease in DOX nuclear penetration and potential shunting of DOX into other non-nuclear organelle components. This suggests that FABP with its multiple isoforms, may play a key role in transporting lipid components into cell nuclei. It also suggests that myristic acid plays a pivotal role in facilitating DOX trafficking into nuclei.

The selected mitochondrial drug delivery by PLN may find some applications in the treatment of mitochondrial dysfunctional diseases, including, neurodegenerative, neuromuscular diseases, diabetes, obesity, migraine and cancer [60–62]. Although there is significant progress in recent years to identify mitochondrial drugs and drug targets, there is a need for developing efficient carrier systems that can selectively deliver drugs to intracellular compartments including mitochondria. Our work suggests that one

may select appropriate lipid and polymer combinations to design PLN for such applications.

3.5. Intra-tumoral localization of PLN in tumor-bearing mice

Initially, intra-tumoral distribution of different compartments of PLN was examined in a murine EMT6 breast tumor model treated with intravenous (i.v.) injection of PLN made from different dye-labeled lipid and polymer. At 1 or 4 h post treatment, tumors were dissected, and tumor slides were prepared for *ex vivo* fluorescence microscopic imaging. As seen in Figure 4A, both components of PLN the FITC-labeled myristic acid and Cy5-labeled-HPESO penetrated through the solid tumor tissue over time. The lipid components are shown more prominently after 1 h post i.v. injection than 4 h, implying progressive transport of DOX cargo by lipid-rich component deep within the tumor.

We further investigated the intracellular distribution of each component of the PLNs *in vitro* using PLN made of FITC-labeled myristic acid and Cy5-amine-labeled HPESO (Cy5-PLN). As shown in (Figure 4B), the lipid component (green) largely circumscribed the nuclei and cytoplasm, and HPESO (red) dispersed within cytoplasm. These results suggest that the lipid may play a critical role in PLN intracellular transport of DOX either to mitochondria or nuclei. Both the *in vitro* and *ex vivo* microscopic examinations demonstrated the dissociation of the PLN, separation of HPESO from the lipid, and their differential trafficking in the tumor tissue and within the cells.

To investigate the intra-tumoral penetration of DOX delivered by various carriers/vehicles, mice bearing EMT6 tumor were injected i.v. with free DOX, DOX-PLN, or commercially available liposomal DOX formulation (Caelyx®). After 1, 4 or 24 h post treatment, tumors were excised, histologic sections were prepared, and fluorescence images were acquired under a fluorescence microscope (Figure 5A–C). The percent of DOX positive areas in the viable tumor tissue at different times was calculated (Figure 5D) and the distance of DOX penetration from a proximal blood vessel was quantified by processing images with a custom MATLAB program (Figure 5E). As seen in Figure 5D, the DOX accumulation in the tumor at 4 h increased by 125% and 39% for DOX-PLN, when compared to free DOX and Caelyx® treatments, respectively. Despite higher accumulation at 1 h post administration, free DOX signal was significantly decreased after 4 h, attributable to rapid elimination of the small molecule drug. In contrast, DOX-PLN treatment increased tumor penetration and retention of DOX even after 24 h, exceeding Caelyx® and free DOX accumulation by 56 and 200%, respectively (Figure 5B).

The average distance of DOX accumulation from the nearest blood vessel was also measured using a customized MATLAB program (Figure 5E). Surprisingly, after 4 h post administration of 25 mg/kg of DOX-equivalent drug/formulation, neither free DOX nor Caelyx® penetrated tumor tissues as deeply as DOX-PLN treatment. The DOX-PLN traveled a distance more than 1.3 to 4-fold from the closest blood vessel at 4 h, when compared to

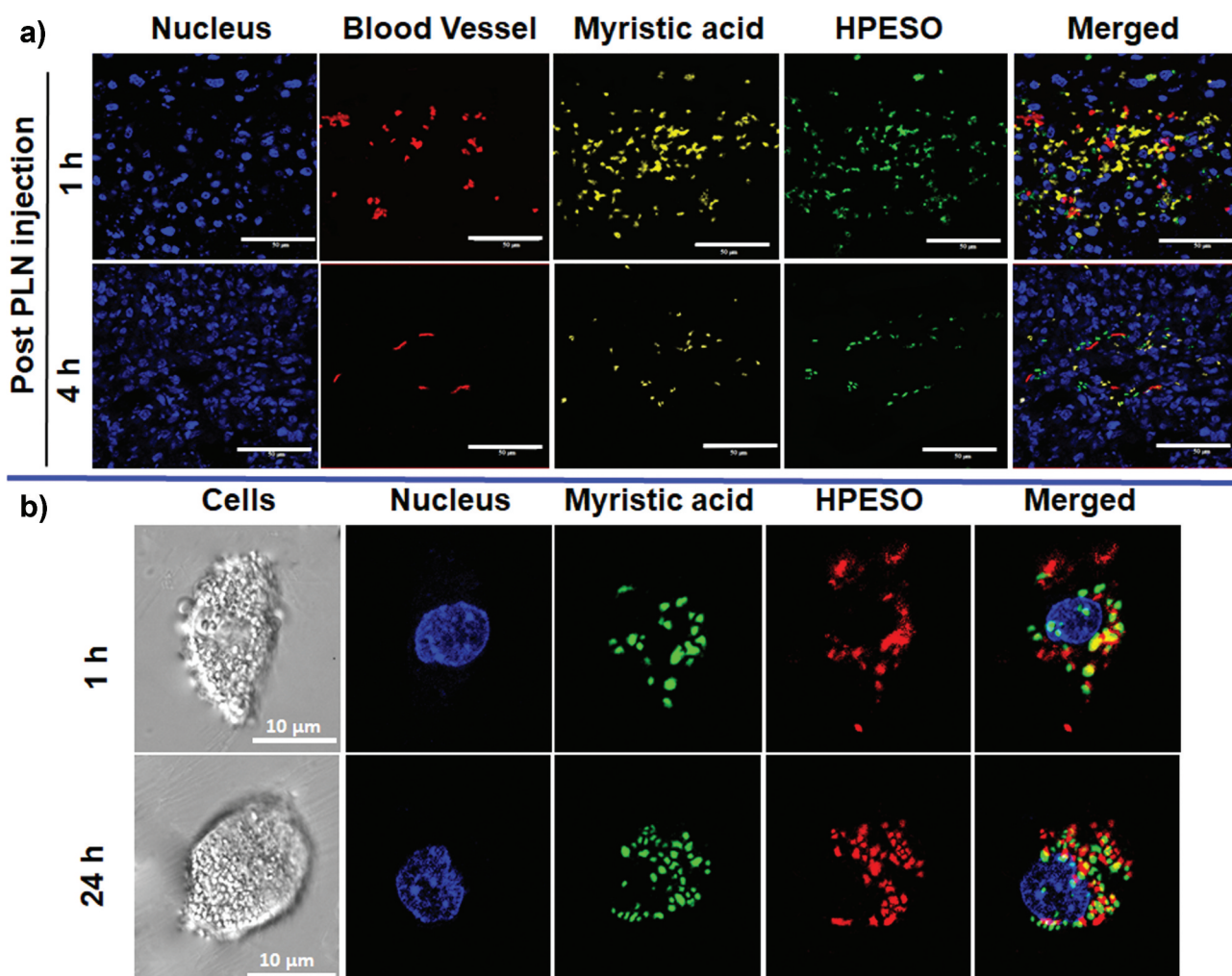


Figure 4. A) Fluorescent image of intra-tumoral localization of PLN at 1 and 4 h post-i.v. injection in EMT6 tumor-bearing mice (nuclei (blue), blood vessel (red), myristic acid (yellow), and HPESO (green)). Scale bar = 50 μm. B) CLSM images of intracellular fate of PLN components (green: FITC-labeled myristic acid; red: Cy5-labeled HPESO) with respect to the nucleus position (stained blue with DAPI) in MDA-MB-231 cells. Cells were incubated with PLNs for 1 or 24 h. Scale bar = 10 μm.

free DOX and Caelyx® treatment groups (Figure 5E). These results suggest that transformable physicochemical properties of PLN may facilitate deeper tumor penetration and longer retention of DOX in the tumor tissue.

4. Conclusion

A transformable PLN system has been designed using a rationally selected lipid combined with a biocompatible polymer. The myristic acid-based PLN underwent time-dependent reduction in particle size and shape change from smooth spheres to spikes in physiological conditions. The DOX-PLN exhibited pH-dependent DOX release with a higher rate at acidic pH of tumor microenvironment and lysosome. The transformation of PLN affected cellular uptake and intracellular localization of PLN components. Confocal microscopy revealed the tendency of lipid component to enter the nuclei more than the polymer component likely due to its small needle shape, shown in the TEM images. *In vitro* inhibition test suggested that clathrin-dependent endocytosis mediated cellular uptake of the unchanged PLN. Lipid mediated transport and interaction of

fatty acid component with FABP7 may play a role in the intracellular trafficking of DOX-PLN and preferential DOX accumulation into the mitochondria and nuclei. ‘Capping’ the carboxylate group of myristic acid with fluorescent dyes reduced DOX transport to mitochondria and nuclei; whereas FABP-7 knock-down decreased DOX accumulation in the mitochondria but did not affect its nuclear deposition compared to that in the wild-type human triple negative MDA-MB-231 cell line. The transformability of PLN facilitated deeper tumor penetration and longer retention of DOX following intravenous administration of DOX-PLN in an orthotopic breast tumor model, as compared with non-transformable liposomal DOX.

The results of this work demonstrated that differential physicochemical properties of lipid and polymer and lipid-FABP interaction can be exploited to construct PLN with desired transformability to achieve effective drug delivery to targeted cellular compartments, thus enhancing its pharmacological effect. The findings of this work suggest that collective consideration of interplay of nanomaterials and cell biology can help the design of NP drug carriers to overcome multi-stage biological barriers for improving cancer chemotherapy. In

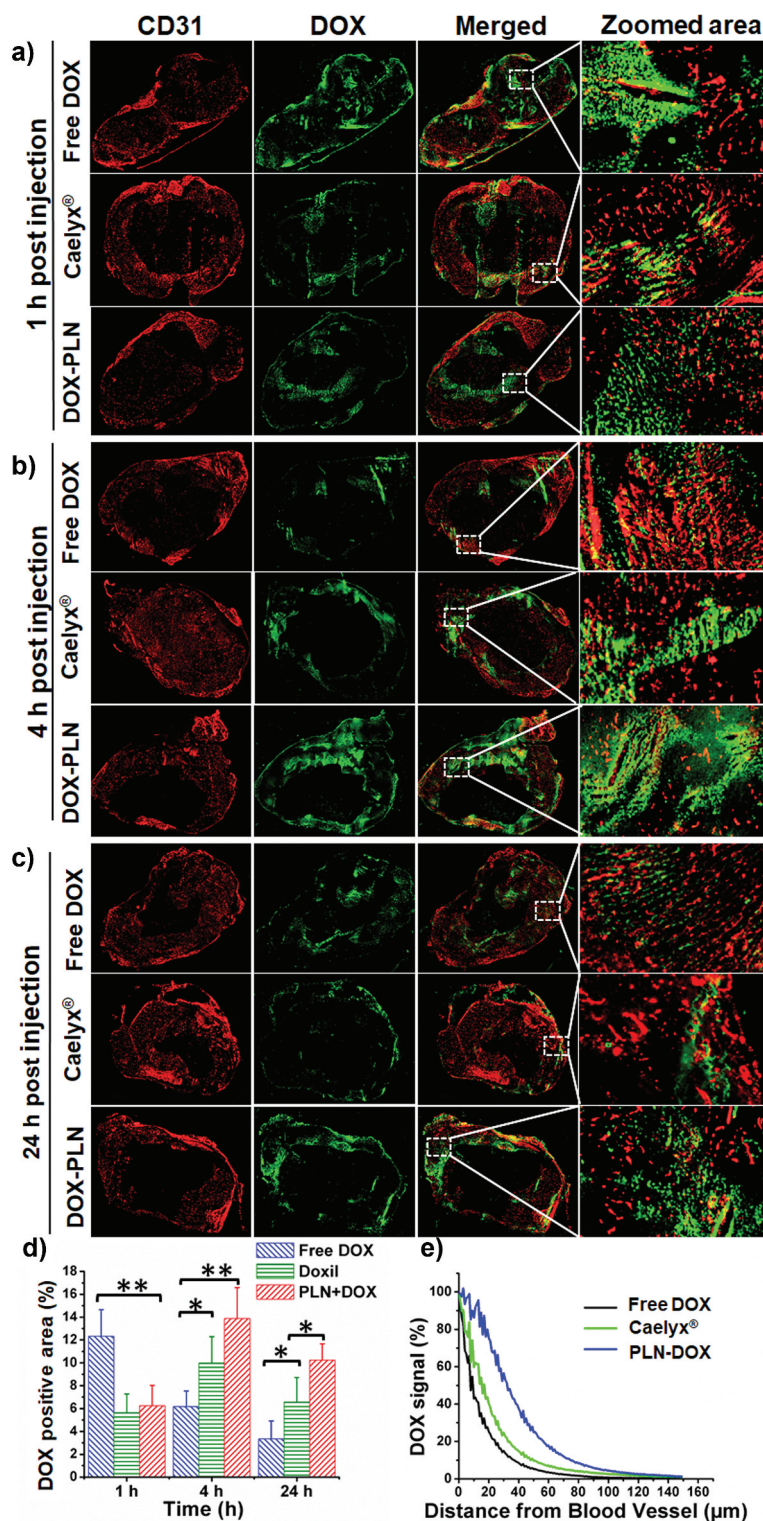


Figure 5. Intra-tumoral accumulation profile of DOX-PLN. A-C) Representative fluorescence images of EMT6 cell bearing orthotopic murine breast tumor sections from mice treated with i.v. administered of free DOX, Caelyx®, or DOX-PLN, equivalent dose of DOX (25 mg/kg) obtained at 1 h (A), 4 h (B) and 24 h (C) post injection. Blood vessels were stained with Anti-CD31-conjugated Alexa Fluor 555. D) Quantification of DOX-positive tumor areas at 1, 4, and 24 h after treatment. E) Percentage of the DOX signal from a proximal blood vessel for different treatment groups at 4 h after injection was obtained using a customized MATLAB program. Texas red (dextran) was injected 20 min before euthanizing animals. Mice were sacrificed 1, 4, and 24 h after injection, and tumors were removed and embedded immediately in octanol compound, frozen in liquid nitrogen, and stored at 70°C.

addition, transformable PLN systems can be engineered to deliver different therapeutic agents for the treatment of other diseases such as those with mitochondrion dysfunction.

Further studies are required to better understand the role of each component of the PLN building blocks in the biofate of the drug cargos especially at the intracellular levels. Thorough

characterization of polymer–lipid interactions is also necessary for the rational design of PLN formulations that can provide desirable changes in the particle size, shape and surface properties, thereby achieving high precision drug delivery.

Acknowledgments

The authors gratefully thank the Canadian Institutes of Health Research (CIHR) for an Operating Grant to XY Wu, AM Rauth, and JT Henderson and the Natural Sciences and Engineering Research Council (NSERC) of Canada for equipment grants to XY Wu; Connaught International Scholarship for Doctoral students and top up scholarship from the Graduate Department of Pharmaceutical Sciences, University of Toronto to T Ahmed and Canada Graduate Scholarship-Doctoral Program (CGS D) from the Natural Sciences and Engineering Research Council of Canada (NSERC) to CD Soeandy.

Reviewer disclosures

Peer reviewers on this manuscript have no relevant financial or other relationships to disclose.

Declaration of interest

The authors have no relevant affiliations or financial involvement with any organization or entity with a financial interest in or financial conflict with the subject matter or materials discussed in the manuscript. This includes employment, consultancies, honoraria, stock ownership or options, expert testimony, grants or patents received or pending, or royalties.

References

Papers of special note have been highlighted as either of interest (*) or of considerable interest () to readers.**

- Shi J, Kantoff PW, Wooster R, et al. Cancer nanomedicine: progress, challenges and opportunities. *Nat Rev Cancer*. 2017;17(1):20–37.
- Wang AZ, Langer R, Farokhzad OC. Nanoparticle delivery of cancer drugs. *Annu Rev Med*. 2012;63(1):185–198.
- Zhang RX, Ahmed T, Li LY, et al. Design of nanocarriers for nanoscale drug delivery to enhance cancer treatment using hybrid polymer and lipid building blocks. *Nanoscale*. 2017;9(4): 1334–1355.
 - **Presents a comprehensive overview of polymer lipid hybrid nanoparticle system. Provides a brief history of PLN development, list of polymer and lipids to rational design of a PLN, advantages of PLN system, and their biological applications.**
- Zhang RX, Wong HL, Xue HY, et al. Nanomedicine of synergistic drug combinations for cancer therapy - strategies and perspectives. *J Control Release*. 2016;240:489–503.
 - **Highlights the effect of synergistic drug combination in cancer chemotherapy. Describes the rationale, principles and advantages of using synergistic drug combination for clinical applications. Provides an insight of rationally designing nanocarriers loaded with wide variety of small molecules and biologics with a synergistic drug combination.**
- Spencer DS, Puranik AS, Peppas NA. Intelligent nanoparticles for advanced drug delivery in cancer treatment. *Curr Opin Chem Eng*. 2015;7:84–92.
- Albanese A, Tang PS, Chan WC. The effect of nanoparticle size, shape, and surface chemistry on biological systems. *Annu Rev Biomed Eng*. 2012;14(1):1–16.
- Yoo JW, Irvine DJ, Discher DE, et al. Bio-inspired, bioengineered and biomimetic drug delivery carriers. *Nat Rev Drug Discov*. 2011;10(7):521–535.
- Barua S, Mitragotri S. Challenges associated with penetration of nanoparticles across cell and tissue barriers: a review of current status and future prospects. *Nano Today*. 2014;9(2):223–243.
- Wilhelm S, Tavares AJ, Dai Q, et al. Analysis of nanoparticle delivery to tumours. *Nat Rev Mater*. 2016;1(5):16014.
- Wang J, Byrne JD, Napier ME, et al. More effective nanomedicines through particle design. *Small*. 2011;7(14):1919–1931.
- Kinnear C, Moore TL, Rodriguez-Lorenzo L, et al. Form follows function: nanoparticle shape and its implications for nanomedicine. *Chem Rev*. 2017;117(17):11476–11521.
- Anselmo AC, Mitragotri S. Impact of particle elasticity on particle-based drug delivery systems. *Adv Drug Deliv Rev*. 2017 1;Jan(108):51–67.
- Blanco E, Shen H, Ferrari M. Principles of nanoparticle design for overcoming biological barriers to drug delivery. *Nat Biotechnol*. 2015;33(9):941–951.
- Cabral H, Matsumoto Y, Mizuno K, et al. Accumulation of sub-100 nm polymeric micelles in poorly permeable tumours depends on size. *Nat Nanotechnol*. 2011;6(12):815–823.
- Duan X, Li Y. Physicochemical characteristics of nanoparticles affect circulation, biodistribution, cellular internalization, and trafficking. *Small*. 2013;9(9–10):1521–1532.
- Sawant RR, Torchilin VP. Challenges in development of targeted liposomal therapeutics. *Aaps J*. 2012;14(2):303–315.
- Allen TM, Cullis PR. Liposomal drug delivery systems: from concept to clinical applications. *Adv Drug Deliv Rev*. 2013 Jan;65(1):36–48.
- Gustafson HH, Holt-Casper D, Grainger DW, et al. Nanoparticle uptake: the phagocyte problem. *Nano Today*. 2015;10(4):487–510.
- Mitragotri S, Lahann J. Physical approaches to biomaterial design. *Nat Mater*. 2009;8(1):15–23.
- Yoo JW, Doshi N, Mitragotri S. Adaptive micro and nanoparticles: temporal control over carrier properties to facilitate drug delivery. *Adv Drug Deliv Rev*. 2011;63(14–15):1247–1256.
 - **Highlights the importance of physicochemical properties of nanoparticles (e.g. size, shape and surface charge) and their impact on drug delivery for cancer therapy.**
- Da Silva-Candal A, Brown T, Krishnan V, et al. Shape effect in active targeting of nanoparticles to inflamed cerebral endothelium under static and flow conditions. *J Control Release*. 2019 Sep;10(309):94–105.
- Yoo J-W MS, Mitragotri S. Polymer particles that switch shape in response to a stimulus. *Proc Natl Acad Sci U S A*. 2010;107(25):11205–11210.
- Hwang DK, Oakey J, Toner M, et al. Stop-flow lithography for the production of shape-evolving degradable microgel particles. *J Am Chem Soc*. 2009;131(12):4499–4504.
- Chien M-P, Rush AM, Thompson MP, et al. Programmable shape-shifting micelles. *Angew Chem (Int Ed in English)*. 2010;49(30):5076–5080.
- Wong HL, Bendayan R, Rauth AM, et al. Chemotherapy with anticancer drugs encapsulated in solid lipid nanoparticles. *Adv Drug Deliv Rev*. 2007;59(6):491–504.
 - **Summarizes the design concept of solid lipid nanoparticles in enhancing cancer chemotherapy.**
- Wu XY. Strategies for optimizing polymer-lipid hybrid nanoparticle-mediated drug delivery. *Expert Opin Drug Deliv*. 2016;13(5):609–612.
- Zhang RX, Li J, Zhang T, et al. Importance of integrating nanotechnology with pharmacology and physiology for innovative drug delivery and therapy - an illustration with firsthand examples. *Acta Pharmacol Sin*. 2018 May;39(5):825–844.
- Wong HL, Bendayan R, Rauth AM, et al. A mechanistic study of enhanced doxorubicin uptake and retention in multidrug resistant breast cancer cells using a polymer-lipid hybrid nanoparticle system. *J Pharmacol Exp Ther*. 2006;317(3):1372–1381.
- Wong HL, Bendayan R, Rauth AM, et al. Development of solid lipid nanoparticles containing ionically complexed chemotherapeutic drugs and chemosensitizers. *J Pharm Sci*. 2004 Aug;93(8):1993–2008.

30. Wong HL, Rauth AM, Bendayan R, et al. A new polymer-lipid hybrid nanoparticle system increases cytotoxicity of doxorubicin against multidrug-resistant human breast cancer cells. *Pharm Res*. 2006;23(7):1574–1585.
31. Wong HL, Bendayan R, Rauth AM, et al. Simultaneous delivery of doxorubicin and GG918 (Elacridar) by new polymer-lipid hybrid nanoparticles (PLN) for enhanced treatment of multidrug-resistant breast cancer. *J Control Release*. 2006;116(3):275–284.
32. Prasad P, Cheng J, Shuhendler A, et al. A novel nanoparticle formulation overcomes multiple types of membrane efflux pumps in human breast cancer cells. *Drug Deliv Transl Res*. 2012;2(2):95–105.
33. Prasad P, Shuhendler A, Cai P, et al. Doxorubicin and mitomycin C co-loaded polymer-lipid hybrid nanoparticles inhibit growth of sensitive and multidrug resistant human mammary tumor xenografts. *Cancer Lett*. 2013;334(2):263–273.
34. Zhang T, Prasad P, Cai P, et al. Dual-targeted hybrid nanoparticles of synergistic drugs for treating lung metastases of triple negative breast cancer in mice. *Acta Pharmacol Sin*. 2017;38(6):835–847.
35. Shuhendler AJ, Prasad P, Zhang RX, et al. Synergistic nanoparticle drug combination overcomes multidrug resistance, increases efficacy, and reduces cardiotoxicity in a nonimmunocompromised breast tumor model. *Mol Pharm*. 2014;11(8):2659–2674.
- **Studies demonstrated that combination of doxorubicin and mitomycin C loaded PLN showed synergistic effect in multidrug resistance (MDR) breast tumor phenotype.**
36. Zhang RX, Cai P, Zhang T, et al. Polymer-lipid hybrid nanoparticles synchronize pharmacokinetics of co-encapsulated doxorubicin-mitomycin C and enable their spatiotemporal co-delivery and local bioavailability in breast tumor. *Nanomedicine*. 2016 Jul;12(5):1279–1290.
37. Xiong XB, Mahmud A, Uludag H, et al. Multifunctional polymeric micelles for enhanced intracellular delivery of doxorubicin to metastatic cancer cells. *Pharm Res*. 2008 Nov;25(11):2555–2566.
38. Baguley BC. Multiple drug resistance mechanisms in cancer. *Mol Biotechnol*. 2010 Nov;46(3):308–316.
39. Ozben T. Mechanisms and strategies to overcome multiple drug resistance in cancer. *FEBS Lett*. 2006 May 22;580(12):2903–2909.
40. Alshareeda AT, Rakha EA, Nolan CC, et al. Fatty acid binding protein 7 expression and its sub-cellular localization in breast cancer. *Breast Cancer Res Treat*. 2012;134(2):519–529.
41. Smathers RL, Petersen DR. The human fatty acid-binding protein family: evolutionary divergences and functions. *Hum Genomics*. 2011 Mar;5(3):170–191.
42. Furuhashi M, Hotamisligil GS. Fatty acid-binding proteins: role in metabolic diseases and potential as drug targets. *Nat Rev Drug Discov*. 2008;7(6):489–503.
43. Zhang RX, Li LY, Li J, et al. Coordinating biointeraction and bioreaction of a nanocarrier material and an anticancer drug to overcome membrane rigidity and target mitochondria in multidrug-resistant cancer cells. *Adv Funct Mater*. 2017;27(39):1700804.
44. Abdekhodaie MJ, Liu Z, Erhan SZ, et al. Characterization of novel soybean-oil-based thermosensitive amphiphilic polymers for drug delivery applications. *Poly Int*. 2012;61(9):1477–1484.
45. Wong HL, Rauth AM, Bendayan R, et al. In vivo evaluation of a new polymer-lipid hybrid nanoparticle (PLN) formulation of doxorubicin in a murine solid tumor model. *Eur J Pharm Biopharm*. 2007 Mar;65(3):300–308.
46. Fan HY, Raval G, Shalviri A, et al. Coupled equilibria of a self-associating drug loaded into polymeric nanoparticles. *Methods*. 2015;76:162–170.
47. Li J, Chu MK, Lu B, et al. Enhancing thermal stability of a highly concentrated insulin formulation with Pluronic F-127 for long-term use in microfabricated implantable devices. *Drug Deliv Transl Res*. 2017 Aug;7(4):529–543.
48. GhavamiNejad A, Lu B, Samarikhalaj M, et al. Transdermal delivery of a somatostatin receptor type 2 antagonist using microneedle patch technology for hypoglycemia prevention. In: *Drug Delivery Transl Res (In Press)*. 2021. <https://doi.org/10.1007/s13346-021-00944-3>.
49. Chithrani BD, Ghazani AA, Chan WCW. Determining the size and shape dependence of gold nanoparticle uptake into mammalian cells. *Nano Lett*. 2006;6(4):662–668.
50. Chithrani BD, Chan WCW. Elucidating the mechanism of cellular uptake and removal of protein-coated gold nanoparticles of different sizes and shapes. *Nano Lett*. 2007;7(6):1542–1550.
51. Barua S, Yoo J-W, Kolhar P, et al. Particle shape enhances specificity of antibody-displaying nanoparticles. *Proc Natl Acad Sci*. 2013;110(9):3270–3275.
52. Ahmed T, Kamel AO, Wettig SD. Interactions between DNA and Gemini surfactant: impact on gene therapy: part I. *Nanomedicine (Lond)*. 2016 Feb;11(3):289–306.
53. Wang Z, Zhang RX, Zhang T, et al. In situ proapoptotic peptide-generating rapeseed protein-based nanocomplexes synergize chemotherapy for Cathepsin-B overexpressing breast cancer. *ACS Appl Mater Interfaces*. 2018 Dec 5;10(48):41056–41069.
54. Shalviri A, Cai P, Rauth AM, et al. Evaluation of new bi-functional terpolymeric nanoparticles for simultaneous in vivo optical imaging and chemotherapy of breast cancer. *Drug Deliv Transl Res*. 2012;2(6):437–453.
55. Shalviri A, Chan HK, Raval G, et al. Design of pH-responsive nanoparticles of terpolymer of poly(methacrylic acid), polysorbate 80 and starch for delivery of doxorubicin. *Colloids Surf B Biointerfaces*. 2013;101:405–413.
56. Behzadi S, Serpooshan V, Tao W, et al. Cellular uptake of nanoparticles: journey inside the cell. *Chem Soc Rev*. 2017 Jul 17;46(14):4218–4244.
57. Rejman J, Oberle V, Zuhorn IS, et al. Size-dependent internalization of particles via the pathways of clathrin- and caveolae-mediated endocytosis. *Biochem J*. 2004;377(Pt 1):159–169.
58. Chamberlain GR, Tulumello DV, Kelley SO. Targeted delivery of doxorubicin to mitochondria. *ACS Chem Biol*. 2013;8(7):1389–1395.
59. Dunn KW, Kamocka MM, McDonald JH. A practical guide to evaluating colocalization in biological microscopy. *Am J Physiol Cell Physiol*. 2011;300(4):C723–42.
60. Fard JK, Hamzeiy H, Sattari M, et al. Triazole rizatriptan induces liver toxicity through lysosomal/mitochondrial dysfunction. *Drug Res (Stuttg)*. 2016 Sep;66(9):470–478.
61. Eftekhari A, Maleki Dizaj S, Sharifi S, et al. The use of nanomaterials in tissue engineering for cartilage regeneration; current approaches and future perspectives. In *Int J Mol Sci*. Vol. 21. Jan 14. 2020;21(2):536. <https://doi.org/10.3390/ijms21020536>.
62. Nunnari J, Suomalainen A. Mitochondria: in sickness and in health. *Cell*. 2012;148(6):1145–1159.